Annals of Biomedical Engineering, Vol. 25, pp. 604–619, 1997
Printed in the USA. All rights reserved.

0090-6964/97 $10.50 + .00

Nonlinear Model for Capillary-Tissue Oxygen Transport and Metabolism

ZHENG LI, TADA YIPINTSOI, and JAMES B. BASSINGTHWAIGHTE

Center for Bioengineering, University of Washington, Seattle, WA

Abstract—Oxygen consumption in small tissue regions cannot be measured directly, but assessment of oxygen transport and metabolism at the regional level is possible with imaging techniques using tracer ^{15}O-oxygen for positron emission tomography. On the premise that mathematical modeling of tracer kinetics is the key to the interpretation of regional concentration-time curves, an axially-distributed capillary-tissue model was developed that accounts for oxygen convection in red blood cells and plasma, nonlinear binding to hemoglobin and myoglobin, transmembrane transport among red blood cells, plasma, interstitial fluid and parenchymal cells, axial dispersion, transformation to water in the tissue, and carriage of the reaction product into venous effluent. Computational speed was maximized to make the model useful for routine analysis of experimental data. The steady-state solution of a parent model for nontracer oxygen governs the solutions for parallel-linked models for tracer oxygen and tracer water. The set of models provides estimates of oxygen consumption, extraction, and venous pO_2 by fitting model solutions to experimental tracer curves of the regional tissue content or venous outflow. The estimated myocardial oxygen consumption for the whole heart was in good agreement with that measured directly by the Fick method and was relatively insensitive to noise. General features incorporated in the model make it widely applicable to estimating oxygen consumption in other organs from data obtained by external detection methods such as positron emission tomography.

Keywords—Nonlinear modeling, Convection, Diffusion, Permeation, Binding, Metabolic reaction, Heart, Myocardial blood flow, Heterogeneity, PET.

INTRODUCTION

Because oxygen usage cannot be measured directly within parts of organs, we must take refuge in indirect methods. Mathematical modeling of oxygen transport and transformation helps by providing quantitative understanding of the physicochemical events. Modeling at the microcirculatory level describes the passage of oxygen molecules to and from the red blood cells (RBCs), through plasma, vascular wall, and extracellular and intracellular space to mitochondria. Details of fluid dynamics and mitochondrial oxygen transport can be neglected while obtaining a good understanding of the kinetics. The Krogh model (34), a single cylindrical tissue unit supplied by a single capillary, has been the basis of most theoretical studies of oxygen transport to tissue over the past 70 years. Other models based on non-Krogh geometry have been designed to reflect the morphological structure of specific tissues (26,31,38,50).

The Krogh cylinder model has no permeability barrier, but incorporates radial diffusion and axial gradients; thus, Krogh, building up the equation of Bohr (13), pioneered the use of spatially distributed models that contrasted with the lumped compartmental models used earlier. Distributed models account for spatial gradients of oxygen concentration, and are described by a set of partial differential equations with respect to time and spatial ordinates. Compartmental models deal with exchanges between wholly mixed domains, with a single value of concentration for each compartment. Compartmental models are described by ordinary differential equations or algebraic equations.

To model high resolution tracer transient data, one needs a physiologically realistic, computationally efficient model. Zierler (52) reported the inadequacy of compartmental models for describing such data. The compartmental models used in dynamic positron emission tomography (PET) studies of cerebral oxygen utilization (30,40,48,49) are overly simplified and do not incorporate nonlinear oxygen binding explicitly. Steady-state models at the cellular and subcellular levels (24,25,35,39) cannot be used to analyze tracer transients. The models by Reneau *et al.* (41) and Bassingthwaighte *et al.* (3) take into account both axial and radial diffusion, but are costly computationally because of the finite difference methods used. The linear axially-distributed model by Rose and Goresky (44) gives good descriptions of tracer transients for oxygen, but does not distinguish erythrocytes from plasma, nor account for the formation of tracer-labeled water. Deussen and Bass-

---

Acknowledgment—The authors appreciate the help of J. E. Lawson in the preparation of this manuscript. The research was supported by the National Institutes of Health Grant RR 1243 (Simulation Resource for Circulatory Mass Transport and Exchange). Experimental data were obtained with the support of the National Institutes of Health Grant HL 50238. Dr. Z. Li was supported by Training Grant HL 07403.

Address correspondence to James B. Bassingthwaighte, Center for Bioengineering, University of Washington, Box 357962, Seattle, WA 98195-7962, U.S.A.

(Received 5Feb96, Revised 4Nov96, Accepted 2Dec96)

ingthwaighte (19) extended the linear models into a dual-species multicapillary model to account for both ^{15}O-oxygen and ^{15}O-water. Virtual volumes of distribution account for the nonlinear binding of oxygen to hemoglobin and myoglobin, RBCs and plasma are lumped together in the vascular space, and oxygen consumption is a first-order reaction in parenchymal cells. The problem in dealing with virtual rather than real volumes is that average partial pressures of oxygen in the intravascular and extravascular spaces have to be estimated to calculate the virtual volumes; so, iterated solutions—based on arterial $p\mathrm{O}_2$, flow, and consumption—are required for curve fitting. Because the virtual volumes change with $p\mathrm{O}_2$ along the length of the capillary and because RBC velocities are higher than plasma velocities in small vessels, a more complete nonlinear model is now presented as a reference standard.

The model is a nonlinear, axially-distributed cylindrical model with capillary and cell permeability barriers and intracellular metabolism of oxygen. Its purposes are: (i) to give a physiologically realistic description of oxygen exchange and metabolic processes in the microcirculation accounting for convective and transmembrane transport, nonlinear binding of oxygen to hemoglobin and myoglobin, transformation in tissue, and axial dispersion (including axial dispersion in vascular space and in tissue); (ii) to achieve high computational efficiency so that many sets of regional experimental data curves from positron emission tomographic imaging can be analyzed; and (iii) to allow exploration and prediction of oxygen transport kinetics under varied physiological and pathological conditions.

THEORY AND METHODS

The Double-Species Capillary-Tissue Unit

The geometry of the model (Fig. 1) is similar to the geometry of a Krogh model. There are four concentric regions: RBCs; plasma; interstitial fluid; and parenchymal cells separated by the membrane of RBCs, capillary wall, and parenchymal cell membrane. Radial diffusion (perpendicular to the length of the capillary tissue unit) within a region is assumed to be instantaneous because the diffusion distances are only a few microns; so, concentrations within a region are uniform radially (but not axially). Because there are no radial gradients, the RBCs can equally well be represented as a central column or as dispersed throughout plasma; these forms are mathematically identical. RBCs and plasma move by plug flow, and can have different velocities in the capillary. Axial diffusion terms, *D's*, represent dispersion in the axial direction by all processes (molecular diffusion, velocity profiles, Taylor diffusion, eddies, etc.). Transmembrane transport for oxygen and water is passive (linear and symmetric) and can be represented by linear first-order parameters, the permeability-surface area product (*PS*). Consumption of oxygen and production of water occurs in parenchymal cells only, governed by the gulosity term G_{pc}. This model presents two choices for oxygen consumption: a constant G_{pc} for linear or first-order consumption and a concentration-dependent G_{pc} for Michaelis-Menten kinetics, which is effectively zero-order in regions of high oxygen concentration and first-order in regions of low oxygen concentration. Equilibrium binding is assumed for oxygen bound to hemoglobin and myoglobin.

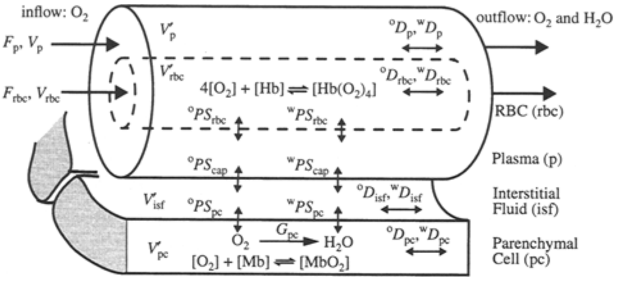

FIGURE 1. Capillary-tissue unit for oxygen transport and metabolism. There are two four-region models in parallel, for oxygen and water, with the transformation occurring only in parenchymal cells. See Table 1 for definitions of the symbols.

The convection-diffusion-consumption model accounts for tracer-labeled oxygen, as well as its metabolic product, water, formed in the parenchymal cell region, the transport of which is accounted for in a separate set of equations.

Based on mass balance, the concentrations of oxygen, $^{\mathrm{o}}C$, and water, $^{\mathrm{w}}C$, with regard to the water space in the four regions are calculated as a function of time (t) and distance (x) along the capillary length (L). For this model, $^{\mathrm{o}}C$ represents the activity or chemical potential for oxygen, equivalent to its partial pressure, in accord with the principle that gradients in partial pressure provide the driving forces for the fluxes. The governing equations for oxygen in four regions are as follows:

in plasma, subscripted p,

$$\frac{\partial^{\mathrm{o}} C_{\mathrm{p}}}{\partial t} = -\frac{F_{\mathrm{p}} L}{V_{\mathrm{p}}} \frac{\partial^{o} C_{\mathrm{p}}}{\partial x} + \frac{{}^{\mathrm{o}}PS_{\mathrm{rbc}}}{{}^{\mathrm{o}}V'_{\mathrm{p}}} ({}^{\mathrm{o}}C_{\mathrm{rbc}} - {}^{\mathrm{o}}C_{\mathrm{p}}) - \frac{{}^{\mathrm{o}}PS_{\mathrm{cap}}}{{}^{\mathrm{o}}V'_{\mathrm{p}}} ({}^{\mathrm{o}}C_{\mathrm{p}} - {}^{\mathrm{o}}C_{\mathrm{isf}}) + {}^{\mathrm{o}}D_{\mathrm{p}} \frac{\partial^{2\mathrm{o}} C_{\mathrm{p}}}{\partial x^2}; \tag{1}$$

in RBCs, subscripted rbc,

$$\frac{\partial({}^{\mathrm{o}}C_{\mathrm{rbc}} + C_{\mathrm{HbO}})}{\partial t} = -\frac{F_{\mathrm{rbc}} L}{V_{\mathrm{rbc}}} \frac{\partial({}^{\mathrm{o}}C_{\mathrm{rbc}} + C_{\mathrm{HbO}})}{\partial x} - \frac{{}^{\mathrm{o}}PS_{\mathrm{rbc}}}{{}^{\mathrm{o}}V'_{\mathrm{rbc}}} ({}^{\mathrm{o}}C_{\mathrm{rbc}} - {}^{\mathrm{o}}C_{\mathrm{p}}) + {}^{\mathrm{o}}D_{\mathrm{rbc}} \frac{\partial^2({}^{\mathrm{o}}C_{\mathrm{rbc}} + C_{\mathrm{HbO}})}{\partial x^2}; \tag{2}$$

in interstitial fluid, subscripted isf,

$$\frac{\partial\, {}^{o}C_{\mathrm{isf}}}{\partial t} = \frac{{}^{o}PS_{\mathrm{cap}}}{{}^{o}V'_{\mathrm{isf}}}\left({}^{o}C_{\mathrm{p}} - {}^{o}C_{\mathrm{isf}}\right) - \frac{{}^{o}PS_{\mathrm{pc}}}{{}^{o}V'_{\mathrm{isf}}}\left({}^{o}C_{\mathrm{isf}} - {}^{o}C_{\mathrm{pc}}\right) + {}^{o}D_{\mathrm{isf}}\frac{\partial^{2}\, {}^{o}C_{\mathrm{isf}}}{\partial x^{2}}; \tag{3}$$

in parenchymal cells, subscripted pc,

$$\frac{\partial({}^{o}C_{\mathrm{pc}} + C_{\mathrm{MbO}})}{\partial t} = \frac{{}^{o}PS_{\mathrm{pc}}}{{}^{o}V'_{\mathrm{pc}}}\left({}^{o}C_{\mathrm{isf}} - {}^{o}C_{\mathrm{pc}}\right) - \frac{G_{\mathrm{pc}}}{{}^{o}V'_{\mathrm{pc}}}\,{}^{o}C_{\mathrm{pc}} + {}^{o}D_{\mathrm{pc}}\frac{\partial^{2}({}^{o}C_{\mathrm{pc}} + C_{\mathrm{MbO}})}{\partial x^{2}}. \tag{4}$$

In these equations, the ${}^{o}V'_{\mathrm{p}}$, ${}^{o}V'_{\mathrm{rbc}}$, ${}^{o}V'_{\mathrm{isf}}$, and ${}^{o}V'_{\mathrm{pc}}$ represent the volume of distribution for dissolved oxygen in these spaces that is assumed to be identical to their water fractions times their anatomic volumes.

The ${}^{o}D$'s represent a combination of molecular diffusion and dispersion due to other factors. ${}^{o}D_{\mathrm{p}}$ represents dispersion in plasma due to molecular diffusion, eddy currents, mixing accompanying erythrocyte rotation and velocity profiles in the presence of rapid radial diffusion. ${}^{o}D_{\mathrm{rbc}}$ mainly represents erythrocyte dispersion. ${}^{o}D_{\mathrm{isf}}$ and ${}^{o}D_{\mathrm{pc}}$ represent a combination of molecular diffusion and irregularities of alignments of capillary-tissue units, whereby, for example, offset positions of starting and ending points of capillaries effectively reduce axial gradients and eliminate the so-called ''lethal corners'' of Krogh cylinder models—those intratissue regions at the downstream end at the periphery of the cylinder. ${}^{o}D_{\mathrm{pc}}$ also represents the combined molecular diffusion of free oxygen and oxymyoglobin (19).

In RBCs, the free oxygen dissolved in the hemoglobin solution is assumed to be in constant equilibrium with oxyhemoglobin; because neither dissociation nor intracellular diffusion are explicitly accounted for, these resistances to oxygen loss from RBCs to plasma are incorporated as limitations to the red cell membrane conductance ${}^{o}PS_{\mathrm{rbc}}$. Each mole of hemoglobin can bind four moles of oxygen. The concentration of oxyhemoglobin is:

$$C_{\mathrm{HbO}} = 4C_{\mathrm{Hbrbc}}S_{\mathrm{Hb}}\,(p), \tag{5}$$

where C_{Hbrbc} is the concentration of hemoglobin in RBC water space; and S_{Hb} is hemoglobin-oxygen saturation. We calculate S_{Hb} according to Adair (53), which is a function of partial pressure (p or pO_2) of oxygen within the RBCs,

$$S_{\mathrm{Hb}}(p) = \mathrm{Adair}\ (p) = \frac{a_1p + 2a_2p^2 + 3a_3p^3 + 4a_4p^4}{4(1 + a_1p + a_2p^2 + a_3p^3 + a_4p^4)}, \tag{6}$$

where p is oxygen partial pressure (pO_2) in hemoglobin solution in torr, and a_1 to a_4 are the Adair coefficients based on human data (Table 1). The Adair equation was chosen instead of Hill's equation because it accurately described the experimental oxyhemoglobin dissociation curve over a wider range of pO_2 (46). One can replace the Adair equation with other empirical formulas (14,45). Using the solubility coefficient, α, p equals ${}^{o}C_{\mathrm{rbc}}/\alpha$, in accord with Henry's law. For the bound oxygen to myoglobin in parenchymal cells, the saturation (S_{Mb}) is calculated using the Hill-type equation,

$$S_{\mathrm{Mb}} = \frac{{}^{o}C_{\mathrm{pc}}/\alpha}{{}^{o}C_{\mathrm{pc}}/\alpha + p50_{\mathrm{Mb}}}. \tag{7}$$

where $p50_{\mathrm{Mb}}$ is the value of pO_2 at which myoglobin is 50% saturated. The oxymyoglobin concentration is:

$$C_{\mathrm{MbO}} = S_{\mathrm{Mb}}C_{\mathrm{Mbpc}}. \tag{8}$$

The governing equations for water are similar to those for oxygen without binding. In addition, a conversion ratio (γ) of labeled oxygen to labeled water is used to account for using different isotopes to label oxygen molecules. Because ^{15}O-oxygen is really ^{15}O-^{16}O, the disappearance of one ^{15}O-oxygen molecule results in the generation of one ^{15}O-labeled water molecule or $\gamma = 1$. For ^{18}O-oxygen, both atoms are labeled; so, $\gamma = 2$. The equations for water are as follows:

in plasma,

$$\frac{\partial\, {}^{w}C_{\mathrm{p}}}{\partial t} = -\frac{F_{\mathrm{p}}L}{V_{\mathrm{p}}}\frac{\partial\, {}^{w}C_{\mathrm{p}}}{\partial x} + \frac{{}^{w}PS_{\mathrm{rbc}}}{V'_{\mathrm{p}}}\left({}^{w}C_{\mathrm{rbc}} - {}^{w}C_{\mathrm{p}}\right) - \frac{{}^{w}PS_{\mathrm{cap}}}{V'_{\mathrm{p}}}\left({}^{w}C_{\mathrm{p}} - {}^{w}C_{\mathrm{isf}}\right) + {}^{w}D_{\mathrm{p}}\frac{\partial^{2}\, {}^{w}C_{\mathrm{p}}}{\partial x^{2}}. \tag{9}$$

in RBCs,

$$\frac{\partial\, {}^{w}C_{\mathrm{rbc}}}{\partial t} = -\frac{F_{\mathrm{rbc}}L}{V_{\mathrm{rbc}}}\frac{\partial\, {}^{w}C_{\mathrm{rbc}}}{\partial x} - \frac{{}^{w}PS_{\mathrm{rbc}}}{V'_{\mathrm{rbc}}}\left({}^{w}C_{\mathrm{rbc}} - {}^{w}C_{\mathrm{p}}\right) + {}^{w}D_{\mathrm{rbc}}\frac{\partial^{2}\, {}^{w}C_{\mathrm{isf}}}{\partial x^{2}}; \tag{10}$$

in interstitial fluid,

$$\frac{\partial\, {}^{w}C_{\mathrm{isf}}}{\partial t} = \frac{{}^{w}PS_{\mathrm{cap}}}{{}^{w}V'_{\mathrm{isf}}}\left({}^{w}C_{\mathrm{p}} - {}^{w}C_{\mathrm{isf}}\right) - \frac{{}^{w}PS_{\mathrm{pc}}}{{}^{w}V'_{\mathrm{isf}}}\left({}^{w}C_{\mathrm{isf}} - {}^{w}C_{\mathrm{pc}}\right) + {}^{w}D_{\mathrm{isf}}\frac{\partial^{2}\, {}^{w}C_{\mathrm{isf}}}{\partial x^{2}}; \tag{11}$$

in parenchymal cells,

$$\frac{\partial {}^{w}C_{pc}}{\partial t} = \frac{{}^{w}PS_{pc}}{{}^{w}V'_{pc}}({}^{w}C_{isf} - {}^{w}C_{pc}) + \gamma \frac{G_{pc}}{{}^{w}V'}\,{}^{w}_{pc}C_{pc} + {}^{w}D_{pc}\frac{\partial^{2w}C_{pc}}{\partial x^{2}}. \tag{12}$$

Steady-State and Transient Solutions for Tracer and Nontracer

The model accounts for both nontracer and tracer-labeled oxygen and water. Because the concentrations of tracer oxygen are orders of magnitude less than nontracer oxygen, the physiological state is not altered by the presence of tracer-labeled oxygen and water. In this model, we assume that nontracer oxygen is in steady-state with constant arterial partial pressure of oxygen (p_A). The model solutions are obtained for both nontracer oxygen at steady-state and tracer transients for oxygen and water. Nontracer oxygen concentration profiles in the four regions determine tracer kinetics. The tracer solution reflects the background oxygen transport and metabolism. Because the kinetics of oxygen is different from the kinetics of the product, water, one can estimate regional oxygen consumption from the tracer transients.

The principle mechanisms for obtaining solutions rapidly are: (i) solving the nontracer steady-state conditions accounting for the nonlinearities and establishing the rate constants for the linearized equations to be solved at each point in space and time; and (ii) using the highly efficient Lagrangian sliding fluid element time-splitting technique to provide analytic solutions for radial exchanges and consumption, and, separately, axial diffusion (10).

Steady-State Solutions for Nontracer Oxygen. First, the model is solved for the steady-state spatial profiles of nontracer oxygen concentrations. These profiles define the conditions for tracer transients and provide the key advantage to the nonlinear modeling, namely providing the correct pO_2 and fractional saturation of binding sites at all positions. In accord with the Lagrangian fluid sliding algorithm used for tracer solutions, the capillary length is divided into N_{seg} segments of equal length, and each segment is assumed to be well-mixed. Mass balance equations are solved for each segment. Governing equations based on mass balance in each of the N_{seg} segments are similar to Eqs. 1 to 4, with left sides set to 0, and by using backward and centered finite difference methods for first- and second-order derivatives.

The boundary conditions for the steady-state equations are as follows:

(i) The inflow oxygen concentrations in RBCs and plasma are:

$$ {}^{n}C^{(0)}_{rbc} = {}^{n}C^{(0)}_{p} = \alpha \cdot p_A, \quad \text{and}$$
$$ {}^{n}C^{(0)}_{HbO} = 4 \cdot C_{Hbrbc} \cdot \text{Adair}\,(p_A). \tag{13}$$

(ii) Reflecting axial diffusion at the ends of the capillary and tissue.

A total of ($5 \times N_{seg}$) equations are solved. Oxymyoglobin concentrations are calculated with Eqs. 7 and 8. Regional concentrations at the succession of axial positions are used to calculate the local volumes of distribution of tracer oxygen at each local pO_2.

Tracer Kinetics. The Lagrangian sliding fluid algorithm (10) is applied for the kinetic equations (Eqs. 1 to 12) for tracer oxygen and water as a function of time and axial position. The time step is the transit time for one segment, $V_p/(F_p \cdot N_{seg})$. At the start of each time step, the fluid contents of each plasma element are advanced by one segment, and the outflow concentration is replaced by that in the last segment. The plasma is the "reference fluid" for the model computations, and volumes of distribution are thus relative to plasma, not blood. The extent to which the fluid element of RBCs moves downstream depends on the ratio of velocities of RBCs to plasma, which is usually observed to be larger than 1 (18,47). In all regions, from RBCs to cells, each segmental region is instantaneously mixed axially and radially. This is the instant of the sliding phase. Thereafter, during that interval, radial exchange between adjacent regions, consumption, axial diffusion, and binding are calculated. Radial exchange and consumption are calculated using a matrix method with a five-term Taylor series as an approximation of the analytic solution. For axial diffusion, different approaches were outlined by Bassingthwaighte *et al.* (8). For equilibrium binding of oxygen to hemoglobin and myoglobin, the local volumes of distribution, ${}^{o}V''$, for the tracer during the transient account for the binding space, and which are therefore greater than the water spaces, ${}^{o}V'$ and ${}^{w}V'$. These are dependent only on the local concentrations of *nontracer* oxygen, not on the tracer, and are calculated as initial conditions. This approach avoids solving nonlinear equations for every segment during every time step, and the exchange matrix needs to be calculated only once after the steady-state solution for *nontracer* oxygen is obtained. Consequently, the computations are fast. In RBCs, V''_{rbc}, the local volume of distribution for oxygen accounting for the binding space is:

$${}^{o}V''_{rbc} = {}^{o}V'_{rbc}\,\frac{{}^{n}C_{rbc} + {}^{n}C_{HbO}}{{}^{n}C_{rbc}}. \tag{14}$$

Note that superscript n here denotes nontracer oxygen, ${}^{o}V'_{rbc}$ is the water space per ml of red cell volume, and the ${}^{o}V''_{rbc}$ is calculated for every segment. The doubly primed symbols ${}^{o}V''_{rbc}$ and ${}^{o}V''_{pc}$ represent the volumes of distribution in erythrocytes and parenchymal cells; actual values for ${}^{o}V''_{rbc}$ and ${}^{o}V''_{pc}$ depend on the local pO_2's and therefore vary with position x/L when there is consumption and with time when there are transients in concentrations of nontracer oxygen. The concentration of total tracer oxygen in RBCs available for transport to plasma or the virtual concentration is:

$$ {}^{o}C'_{rbc} = ({}^{o}C_{rbc} + C_{HbO}) \frac{{}^{o}V'_{rbc}}{{}^{n}V''_{rbc}}. \tag{15} $$

Similarly, in the parenchymal region:

$$ {}^{o}V''_{pc} = {}^{o}V'_{pc} \frac{{}^{n}C_{pc} + {}^{n}C_{MbO}}{{}^{n}C_{pc}} \quad \text{and} $$

$$ {}^{o}C'_{pc} = ({}^{o}C_{pc} + C_{MbO}) \frac{{}^{o}V'_{pc}}{{}^{o}V''_{pc}} \tag{16} $$

Therefore, Eqs. 1 to 4 can be rewritten and solved using ${}^{o}V''_{rbc}$, ${}^{o}V''_{pc}$, ${}^{o}C'_{rbc}$, and ${}^{o}C'_{pc}$.

In summary, local volumes of distribution ${}^{o}V''_{rbc}$ and ${}^{o}V''_{pc}$ are calculated in the initial phase after the steady-state solution for nontracer oxygen is obtained. The virtual concentrations of tracer oxygen in RBCs and parenchymal cells are updated at each time step to be used in radial exchange. Therefore, tracer kinetics are computed in the following sequence.

1. At the start of the time interval, the plasma slides downstream by one segment and RBCs slide by the amount equal to velocity ratio, $r_{vel} = v_{rbc}/v_p$. We interpolate to obtain the mean ${}^{o}C_{rbc}$ and C_{HbO} in each segment.
2. Calculate ${}^{o}C'_{rbc}$ and ${}^{o}C'_{pc}$ from Eqs. 15 and 16.
3. Calculate radial exchange and consumption by the matrix inversion for each segment.
4. Calculate axial diffusional exchanges and the resultant local virtual concentrations.
5. Calculate the chemical concentrations ${}^{o}C_{rbc}$ and C_{HbO} from the virtual concentrations and volumes in the erythrocytes:

$$ {}^{o}C_{rbc} = \frac{{}^{n}C_{rbc}\,{}^{o}C'_{rbc}V''_{rbc}}{({}^{n}C_{rbc} + {}^{n}C_{HbO})V'_{rbc}}, $$

$$ C_{Hbo} = \frac{{}^{n}C_{Hbo}\,{}^{o}C'_{rbc}V''_{rbc}}{({}^{n}C_{rbc} + {}^{n}C_{HbO})V'_{rbc}}. \tag{17} $$

6. Increment time by one step, $dt = (V_p/N_{seg})/F_p$, $t = t + dt$, and return to step 1.

Calculation of Capillary Hematocrit. Erythrocyte mean transit time through the coronary system is less than plasma transit time, because the velocity of RBCs is faster than that of plasma. The ratio of RBCs to plasma velocity, r_{vel}, is reflected in a difference between large vessel hematocrit (Hct) and capillary hematocrit ($\mathrm{Hct_{cap}}$). In this model, the total blood flow, F_B, the capillary volume, V_{cap}, and the velocity ratio, r_{vel}, are given; then, the capillary hematocrit, $\mathrm{Hct_{cap}}$, the RBC volume, V_{rbc}, and the plasma volume, V_p, in the capillary can be derived. The intracapillary RBC flow, F_{rbc}, and plasma flow, F_p, are identical to the large vessel flows and $F_{rbc} = \mathrm{Hct} \cdot F_B$ while $F_p = (1 - \mathrm{Hct}) \cdot F_B$. It follows then, that:

$$ r_{vel} = \frac{F_{rbc}/V_{rbc}}{F_p/V_p}, \tag{18} $$

$$ F_{rbc} = F_B \cdot \mathrm{Hct} \quad \text{and} \quad F_p = F_B \cdot (1 - \mathrm{Hct}), \tag{19} $$

$$ V_{rbc} = V_{cap} \cdot \mathrm{Hct_{cap}} \quad \text{and} \quad V_p = V_{cap} \cdot (1 - \mathrm{Hct_{cap}}), \tag{20} $$

$$ V'_{rbc} = W_{rbc} \cdot V_{rbc} \quad \text{and} \quad V'_p = W_p \cdot V_p, \tag{21} $$

$$ \mathrm{Hct_{cap}} = \frac{\mathrm{Hct}}{(1 - r_{vel})\,\mathrm{Hct} + r_{vel}}. \tag{22} $$

Mean Transit Times and Mean Transit Time Volumes. The key to estimating regional oxygen consumption is the difference between the transit times for water and oxygen. Because the oxygen is highly concentrated in erythrocytes and there is relatively little in the extravascular regions, the transit time for unconsumed oxygen is close to that for erythrocytes. In contrast, the water fraction of blood is similar to that of the extravascular tissue, so that water transit time is the capillary transit time times the ratio of total myocardial water to capillary water. This means that ^{15}O-water retention is long compared with that of ^{15}O-oxygen.

First, for blood, the mean transit time is composed of the sum of transit times through the arteries, capillaries, and veins in series, $\bar{t}_B = \bar{t}_A + \bar{t}_{cap} + \bar{t}_V = (V_A + V_{cap} + V_V)/F_B$, where:

$$ \bar{t}_{cap} = \mathrm{Hct} \cdot \frac{V_{rbc}}{F_{rbc}} + (1 - \mathrm{Hct}) \cdot \frac{V_p}{F_p} = \frac{V_{cap}}{F_B}. \tag{23} $$

For the values given in Table 1, $\bar{t}_A = 1.8$, $\bar{t}_{cap} = 4.25$, and $\bar{t}_V = 3.0$ sec. For the calculation that follows, we use the parameter values in Table 1.

For intracapillary water, the transit time ${}^{w}\bar{t}_{cap}$ differs from $\bar{t}_{cap}$ because the water fractions of RBCs and plasma differ and the velocity ratio v_{rbc}/v_p is normally >1.0. The descriptive statement for ${}^{w}\bar{t}_{cap}$ is $\bar{t}_{rbc}$ · (fraction of capillary water within RBCs) + $\bar{t}_p$ · (fraction of capillary water in plasma). In algebraic terms:

$$ {}^{w}\bar{t}_{cap} = \frac{V_{rbc}}{F_{rbc}} \cdot \frac{\mathrm{Hct}\, W_{rbc}}{\mathrm{Hct}\, W_{rbc} + (1 - \mathrm{Hct})\, W_p} + \frac{V_p}{F_p} \cdot \frac{1 - \mathrm{Hct}\, W_p}{\mathrm{Hct}\, W_{rbc} + (1 - \mathrm{Hct})\, W_p} = \frac{V_{cap}[\mathrm{Hct_{cap}}\, W_{rbc} + (1 - \mathrm{Hct_{cap}})\, W_p]}{F_B[\mathrm{Hct}\, W_{rbc} + (1 - \mathrm{Hct})\, W_p]}, \tag{24} $$

which gives 4.35 sec for intracapillary water transit time, longer than that for blood because the water fraction is higher in the more slowly moving phase.

The water transit time, ${}^{\mathrm{w}}\bar{t}_{\mathrm{ct}}$, when exchange occurs between blood and tissue, is enlarged proportionately to the ratio of total tissue water space to intracapillary water space:

$$ {}^{\mathrm{w}}\bar{t}_{\mathrm{ct}} = \left(\frac{V'_{\mathrm{rbc}} + V'_{\mathrm{p}} + V'_{\mathrm{isf}} + V'_{\mathrm{pc}}}{V'_{\mathrm{rbc}} + V'_{\mathrm{p}}}\right) \cdot {}^{\mathrm{w}}\bar{t}_{\mathrm{cap}}, \qquad (25) $$

which gives 59.45 sec, much longer than the capillary transit time for blood.

In contrast, for oxygen, the mean transit time is close to that of blood. We again start with the generalities:

$$ {}^{\mathrm{o}}\bar{t}_{\mathrm{cap}} = \frac{\text{(total tissue oxygen content)}}{\text{(intracapillary blood oxygen content)}} \cdot \text{(intracapillary oxygen transit time)}. \qquad (26) $$

The intracapillary oxygen transit time ${}^{\mathrm{o}}\bar{t}_{\mathrm{cap}}$ is:

$$ {}^{\mathrm{o}}\bar{t}_{\mathrm{cap}} = \frac{V_{\mathrm{cap}}}{F_{\mathrm{B}}} \times \frac{[({}^{\mathrm{n}}C_{\mathrm{rbc}} + {}^{\mathrm{n}}C_{\mathrm{HbO}})\mathrm{Hct}_{\mathrm{cap}}\, W_{\mathrm{rbc}} + {}^{\mathrm{n}}C_{\mathrm{p}}(1 - \mathrm{Hct}_{\mathrm{cap}})\, W_{\mathrm{p}}]}{[({}^{\mathrm{n}}C_{\mathrm{rbc}} + {}^{\mathrm{n}}C_{\mathrm{HbO}})\mathrm{Hct}\, W_{\mathrm{rbc}} + {}^{\mathrm{n}}C_{\mathrm{p}}(1 - \mathrm{Hct})\, W_{\mathrm{p}}]}, \qquad (27) $$

which gives 3.37 sec for given parameter values (Table 1) at an arterial $p\mathrm{O}_2 = 100$ torr.

The oxygen transit time ${}^{\mathrm{o}}\bar{t}_{\mathrm{ct}}$ for transport through the blood–tissue exchange unit, where there is exchange with tissue but no consumption from Eq. 26, is:

$$ {}^{\mathrm{o}}\bar{t}_{\mathrm{ct}} = \mathrm{Ave}\left[\frac{{}^{\mathrm{o}}V''_{\mathrm{rbc}} + {}^{\mathrm{o}}V'_{\mathrm{p}} + {}^{\mathrm{o}}V_{\mathrm{isf}} + {}^{\mathrm{o}}V''_{\mathrm{pc}}}{{}^{\mathrm{o}}V''_{\mathrm{rbc}} + {}^{\mathrm{o}}V'_{\mathrm{p}}}\right] \cdot {}^{\mathrm{o}}\bar{t}_{\mathrm{cap}}, \qquad (28) $$

where Ave[. . .] indicates the spatial average of the ratio over the length L of the exchange unit. For the zero consumption case, ${}^{\mathrm{o}}\bar{t}_{\mathrm{ct}}$ is 5.46 sec, only a little larger than for the blood oxygen transit time. At a lower arterial $p\mathrm{O}_2$ of 26 torr, still without consumption, the values of ${}^{\mathrm{o}}\bar{t}_{\mathrm{cap}}$ and ${}^{\mathrm{o}}\bar{t}_{\mathrm{ct}}$ are 3.37 and 6.44 sec. At an arterial $p\mathrm{O}_2$ of 2 torr, without consumption, ${}^{\mathrm{o}}\bar{t}_{\mathrm{ct}}$ is longer yet because a larger fraction of the total oxygen is bound to myoglobin.

When oxygen is consumed, two complex events occur to change the apparent transit times. First, the oxygen that is consumed is necessarily that which has entered parenchymal cells, and is that which would have the longest transit times; so, ${}^{\mathrm{o}}\bar{t}_{\mathrm{cap}}$ is reduced because the ratio of the extravascular to the intracapillary volume of distribution is decreased. Second, the estimated ${}^{\mathrm{w}}\bar{t}_{\mathrm{cap}}$, which is appropriate for tracer water entering via the arterial inflow, can change; the water is formed within the tissue and will not traverse the length of the capillary in the absence of axial diffusion. The actual mean transit times can be estimated from the first moments of the model solutions and will be reported in results for specified conditions.

Michaelis-Menten Consumption. If Michaelis-Menten kinetics is used for oxygen consumption, the equivalent G_{pc} term is dependent on the local *nontracer* oxygen concentration,

$$ G_{\mathrm{pc}}^{(\mathrm{i})} = \frac{V_{\mathrm{max}}}{K_{\mathrm{m}} + {}^{\mathrm{n}}C_{\mathrm{pc}}^{(\mathrm{i})}}. \qquad (29) $$

Numerically, the consumption matrix needs to be updated at each time step.

Calculation of Steady-State Extraction, Venous pO_2, and Oxygen Consumption. The model solution gives the outflow nontracer oxygen concentration in RBCs and plasma, so the venous $p\mathrm{O}_2$ (p_{V}) can be calculated by equilibrating oxygen in blood, using Eq. 6 for $S_{\mathrm{Hb}}(p)$ and using the concentrations at the last segment of the capillary, indexed N_{seg}, for nontracer oxygen, giving the venous oxygen concentration, ${}^{\mathrm{o}}C_{\mathrm{V}}$:

$$ \begin{aligned} {}^{o}C_{\mathrm{V}} &= \left({}^{\mathrm{n}}C_{\mathrm{HbO}}^{(N_{\mathrm{seg}})} + {}^{\mathrm{n}}C_{\mathrm{rbc}}^{(N_{\mathrm{seg}})}\right)\mathrm{Hct} \cdot W_{\mathrm{rbc}} + {}^{\mathrm{n}}C_{\mathrm{p}}^{(N_{\mathrm{seg}})}(1 - \mathrm{Hct})\, W_{\mathrm{p}} \\ &= (4C_{\mathrm{Hbrbc}} \cdot S_{\mathrm{Hb}}(p_{\mathrm{V}}) + \alpha \cdot \mathrm{p}_{\mathrm{V}})\,\mathrm{Hct} \cdot W_{\mathrm{rbc}} \\ &\quad + \alpha \cdot p_{\mathrm{V}} \cdot (1 - \mathrm{Hct}) \cdot W_{\mathrm{p}}. \end{aligned} \qquad (30) $$

Oxygen concentration in the arterial inflow is:

$$ \begin{aligned} {}^{\mathrm{o}}C_{\mathrm{A}} &= (4C_{\mathrm{Hbrbc}} \cdot S_{\mathrm{Hb}}\,(p_{\mathrm{A}}) + \alpha \cdot p_{\mathrm{A}})\,\mathrm{Hct} \cdot W_{\mathrm{rbc}} \\ &\quad + \alpha \cdot p_{\mathrm{A}} \cdot (1 - \mathrm{Hct})\, W_{\mathrm{p}}. \end{aligned} \qquad (31) $$

Steady-state extraction (E_{ss}) is $E_{\mathrm{ss}} = ({}^{\mathrm{o}}C_{\mathrm{A}} - {}^{\mathrm{o}}C_{\mathrm{V}})/{}^{\mathrm{o}}C_{\mathrm{A}} \times 100\%$.

Oxygen consumption is calculated by:

$$ \mathrm{MR}_{\mathrm{O}_2} = \frac{1}{N_{\mathrm{seg}}} \sum_{\mathrm{i}=1}^{N_{\mathrm{seg}}} G_{\mathrm{pc}}^{(\mathrm{i})}\, {}^{\mathrm{n}}C_{\mathrm{pc}}^{(\mathrm{i})}, \qquad (32) $$

where $G_{\mathrm{pc}}^{(\mathrm{i})}$ is the rate constant for first-order consumption in the *i*th segment. The estimate should (and must) exactly match the consumption of nontracer oxygen by the Fick calculation:

$$ \mathrm{MR}_{\mathrm{O}_2} = F_B \cdot E_{\mathrm{SS}} \cdot {}^{\mathrm{o}}C_{\mathrm{A}} = F_B({}^{\mathrm{o}}C_{\mathrm{A}} - {}^{\mathrm{o}}C_{\mathrm{V}}). \qquad (33) $$

Single-Pathway Model Configuration

The steady-state spatial distribution of regional blood flows within organs is known to be broad, having coefficients of variations of 25% or more depending on the tissue under study and the ambient humoral, neural, and metabolic conditions (7,9,32). To allow an appropriate description of spatial heterogeneity, the capillary-tissue unit can be incorporated into a multicapillary configuration in which the blood–tissue exchange regions are composed of a set of parallel, independent capillary-tissue units such as those described by King *et al.* (33) or Clough *et al.* (16). This particular model for oxygen transport and metabolism can be used in a similar fashion, but we will con-

TABLE 1. Terminology and parameter values for the oxygen transport model.

Symbol	Name, Definition	Value[a]	Units
a_1	Adair coefficient, $a_1 = (p50_{Hb})^{-0.4948} \times 10^{-1.117}$	0.01524	Unitless
a_2	Adair coefficient, $a_2 = (p50_{Hb})^{0.7473} \times 10^{-5.207}$	7.1×10^{-5}	Unitless
a_3	Adair coefficient, $a_3 = 0$	0	Unitless
a_4	Adair coefficient, $a_4 = (p50_{Hb})^{-3.955} \times 10^{0.0238}$	2.7×10^{-6}	Unitless
^{o}C, $^{o}C'$	Concentration of dissolved oxygen in water space, total oxygen concentration (including bound form) in water space		Molar, mmol ml^{-1} for nontracer; cpm/ml, cps/voxel for tracer
^{w}C	Concentration of water		Molar, mmol ml^{-1} for nontracer; cpm/ml, cps/voxel for tracer
C_{Hbrbc}	Hemoglobin concentration in RBC water space	8.2×10^{-3}	Molar
C_{Mbpc}	Myoglobin concentration in the water space of parenchymal cells	0.5×10^{-3}	Molar
D	Axial dispersion, axial diffusion coefficient	10^{-4}	$cm^2\ sec^{-1}$
E_{ss}	Steady-state extraction of nontracer oxygen	0–1	Unitless
F	Flow	1 (0.2–10)	ml min^{-1} g^{-1}
f_{bm}	Spillover ratio from blood to myocardium		Unitless
G_{pc}	Gulosity coefficient, first-order clearance by consumption	0–300	ml min^{-1} g^{-1}
Hct	Large vessel hematocrit	0.5	Unitless
Hct_{cap}	Capillary hematocrit	0.4	Unitless
$h(t)$	Transport function		sec^{-1}
K_m	Michaelis-Menten constant for oxygen	1×10^{-9}	Molar
L	Capillary length, defining position x, $0 < x < L$	0.1	cm
MR_{O_2}	Metabolic rate for oxygen	0–10	μmol min^{-1} g^{-1}
N_{seg}	Number of segments along the capillary length	10, 30	Unitless
pO_2, p	Oxygen partial pressure	0–650	torr
$p50_{Hb}$	Partial pressure at 50% saturation of hemoglobin	26	torr
$p50_{Mb}$	Partial pressure at 50% saturation of myoglobin	2.5	torr
PS	Permeability-surface area product		ml min^{-1} g^{-1}
$^{o}PS_{rbc}$	PS of red blood cell membrane for oxygen	1,000	ml min^{-1} g^{-1}
$^{o}PS_{cap}$	PS of capillary wall for oxygen	200	ml min^{-1} g^{-1}
$^{o}PS_{pc}$	PS of parenchymal cell membrane for oxygen	2,000	ml min^{-1} g^{-1}
$^{w}PS_{rbc}$	PS of red blood cell membrane for water	100	ml min^{-1} g^{-1}
$^{w}PS_{cap}$	PS of capillary wall for water	100	ml min^{-1} g^{-1}
$^{w}PS_{pc}$	PS of parenchymal cell membrane for water	100	ml min^{-1} g^{-1}
RBC	Red blood cells		
$R(t)$	Residue function		Unitless
r_{vel}	Ratio of RBCs to plasma velocity	1.5	Unitless
S	Saturation of oxygen in hemoglobin, fraction of sites occupied		Unitless
t, $\bar{t}$	Time, mean transit time		sec
V, V', V''	V, anatomical volume; V', volume of distribution excluding binding, normally the water space (no binding); V'', volumes of distribution including the binding space		ml g^{-1}
V_A	Arterial blood volume	0.03	ml g^{-1}
V_{cap}	Capillary volume	0.07	ml g^{-1}
V_{max}	Maximum consumption rate for Michaelis-Menten kinetics	5	μmol min^{-1} g^{-1}
V_V	Volume of blood in veins	0.05	ml g^{-1}
V'_{isf}	Volume of distribution of oxygen or water in interstitial fluid	0.18	ml g^{-1}
V'_{pc}	Volume of distribution of dissolved oxygen or water in parenchymal cells	0.55	ml g^{-1}
W_{isf}, W_{pc}	Fractional water content of interstitial fluid, parenchymal cells pc	0.80	ml/ml
W_{rbc}	Fractional water content of RBCs	0.65	ml/ml
W_p	Fractional water content of plasma	0.94	ml/ml
x	Axial distance from capillary entrance		cm
α	Solubility coefficient for oxygen in water @ 37°C	1.35×10^{-6}	mmol ml^{-1} $torr^{-1}$
γ	Conversion ratio for oxygen to water	1	Unitless
Subscripts		Superscripts	
Hb; HbO	Hemoglobin; oxyhemoglobin	o	Oxygen
Mb, MbO	Myoglobin, oxymyoglobin	w	Water
cap, ct	Capillary, capillary-tissue unit	n	Nontracer
rbc	Red blood cells		
p	Plasma		
pc	Parenchymal cell		
isf	Interstitial fluid		
r	Region (rbc, p, isf, or pc)		
A	Arterial		
V	Venous		
B	Blood		

[a] Value is that used in the simulations, except where indicated for the various figures.

centrate on the capillary-tissue unit that is best explored in a single-pathway model configuration. Two large-vessel units representing the arteries and veins were connected in series with the capillary-tissue exchange unit (computed with 30 axial segments). The large vessel unit is a submodel of the capillary-tissue exchange unit, but consists of RBC and plasma regions with identical velocity.

RESULTS OF COMPUTER SIMULATION

Model parameter values were taken from published data and varied to illustrate model behavior or optimized to fit experimental data. See Table 1 for standard values. The steady-state axial profiles of nontracer oxygen concentration (the nonlinearities of which govern the volumes of distribution for tracer) and the dependent linear kinetics of tracer-labeled oxygen were computed. The effects of blood flow, hematocrit, arterial pO_2, velocity ratio of RBC to plasma, myoglobin binding and axial diffusion were tested by changing their values one at a time.

Choices of Parameter Values

These are listed in the terminology. Here we provide some ancillary information and the rationale for some choices. Mean capillary flow, F_B, was set at 1 ml min^{-1} g^{-1}, a value typical for myocardial blood flows. The capillary volume of the blood–tissue exchange unit, V_{cap}, was set at 0.07 ml g^{-1} from anatomic estimates (4). The volumes of the RBCs and plasma depend on the capillary hematocrit Hct_{cap}, which is different from the large vessel hematocrit Hct if the velocity ratio, r_{vel}, of the red blood cells to plasma is not unity. We chose $r_{vel} = 1.5$, so with Hct = 0.5, $Hct_{cap} = 0.4$ (Eq. 22), $V_{rbc} = 0.028$ ml g^{-1}, and $V_p = 0.042$ ml g^{-1}, giving a hematocrit-dependent water space in the capillary, ${}^{w}V_{cap} = 0.65V_{rbc} + 0.94V_p$ or 0.058 in this particular case. The volumes of distributions for dissolved oxygen are water spaces within each region. The volumes of distribution for the interstitial fluid and parenchymal cells were set to those known for the water space (*i.e.*, $V'_{isf} = 0.18$ ml g^{-1} and $V'_{pc} = 0.55$ ml g^{-1}) (6); so, the total water space is 0.788 in accord with values obtained from tissue water content (54). These volumes applied to both oxygen and water.

Values for the *PS*'s for oxygen and water are so high that they have never been measured accurately. They must be higher than 50 or 100 ml min^{-1} g^{-1} to account for the flow-limited exchange that is observed. This means that their values do *not* influence the shapes of the dilution curves. The *PS* values for oxygen in ml min^{-1} g^{-1} were set at ${}^{o}PS_{rbc} = 1{,}000$, ${}^{o}PS_{cap} = 200$, and ${}^{o}PS_{pc} = 2000$. Note that these values are 2 orders of magnitude larger than the data from Rose and Goresky (44), where they used small values for the virtual volumes in the extravascular space to account for the binding space in the RBCs. The ratio of surface areas for parenchymal cells (36,37,51) and capillary wall (4) is 2,000 cm^2 g^{-1} to 500 cm^2 g^{-1}, but we chose a value of 10 for ${}^{o}PS_{pc}/{}^{o}PS_{cap}$ to account for the fact that the myocyte plasmalemma is a single bilayer, whereas the capillary membrane is composed of the two bilayers of the endothelial cell, the cell itself, and the underlying basement membrane. For water, all *PS* values were set to 100 ml min^{-1} g^{-1}, which is so high that water exchange is flow-limited. Axial dispersion coefficients, ${}^{w}D_{isf}$ and ${}^{w}D_{pc}$, were used as shaping factors. These axial dispersion coefficients, in order to provide a statistical approximation for nonalignment of capillary beginnings and endings and the heterogeneity of local geometry, must be set at values higher than the purely molecular diffusion coefficient for water found by Safford *et al.* (55) in the myocardium. We chose for simplicity ${}^{w}D_{isf} = {}^{w}D_{pc} = {}^{o}D_{isf} = {}^{o}D_{pc} = 10^{-4}$ cm^2 sec^{-1}. Likewise, we assumed ${}^{w}D_p = {}^{o}D_p$ and used these to represent intravascular axial dispersion.

Michaelis-Menten consumption was used and V_{max} was set at 5 μmol min^{-1} g^{-1} and K_m was set to a very small number; hence, the oxygen consumption was constant or zero-order along the capillary length until the local oxygen concentration reached a very low level. The hemoglobin concentration in the RBCs, C_{Hbrbc}, was set at 8.15 mM, which was 35 g/100 ml of RBCs or 5.3 mM divided by the water fraction of RBCs (0.65).

Volumes of large vessels, V_A and V_V, were chosen to be 0.03 and 0.05 ml g^{-1} in accord with the total vascular volumes being between 0.12 and 0.15 ml g^{-1}, including the capillary volume (22). Thus, the large vessel volume, $V_A + V_V$, was 0.08 ml g^{-1}. These parameter values were used in all simulations unless explicitly mentioned otherwise.

Axial Concentration Profiles for Nontracer Oxygen at Steady State

Shown in Fig. 2 are the concentration profiles along the capillary length for the oxyhemoglobin in the RBCs and free oxygen in the RBCs, plasma, and parenchymal cells. There were gradients along the capillary length as well as between regions. Free oxygen concentration decreased exponentially from the upstream to the downstream end, whereas the oxyhemoglobin concentration decayed almost linearly due to the nonlinear nature of the oxygen dissociation curve. The calculated total oxygen consumption, MR_{O_2}, was the same as V_{max} at 5 μmol min^{-1} g^{-1}, indicating there was sufficient oxygen supply throughout the cell region where the consumption occurs.

Forms of Residue and Outflow Curves for ^{15}O-Oxygen Bolus Input

To simulate a bolus injection of tracer oxygen, a lagged normal density function (1) was chosen to represent the

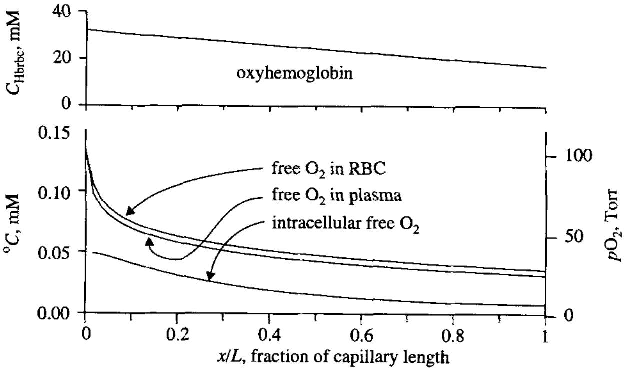

FIGURE 2. Nontracer oxygen concentration profiles along the capillary length at a particular steady state. Zero-order consumption was used with $\mathrm{MR}_{\mathrm{O}_2}$ set to 5 μmol min^{-1} g^{-1}. Axial diffusion was 0. With an arterial $p\mathrm{O}_2$ of 100 torr, the venous $p\mathrm{O}_2$ was 26.7 torr and extraction was 47%.

input concentration-time curve. The normalized input, residue, and outflow dilution curves are shown in Fig. 3. In addition to the sum of labeled oxygen and water, we also plotted labeled oxygen and water separately to reveal their different kinetics. One fraction of oxygen entered the parenchymal cells where most was metabolized to water. The unmetabolized fraction, mostly carried in RBCs, first appeared at the capillary end after 8.1 sec, which effectively equals the RBC mean transit time, $V_{\text{rbc}}/F_{\text{rbc}} + V_{\text{LV}}/F_{\text{B}}$. The metabolic product water reached the outflow later. The total tissue residue curve, $R(t)$, was dominated by the intravascular oxygen content at early times, but was virtually identical to the water residue after 25 sec. The area under the tracer oxygen outflow curve was 53% of the area under the outflow curve for total tracer, which agrees with the steady-state extraction of nontracer oxygen being 47%.

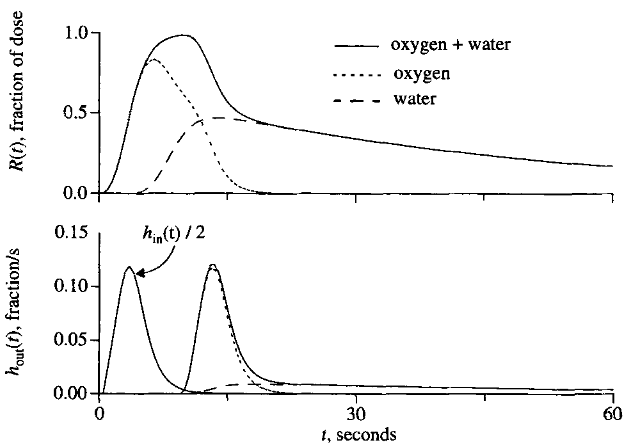

FIGURE 3. The normalized residue (top) and outflow (bottom) dilution curves after a bolus injection of tracer-labeled oxygen. The input function is a lagged normal density function with unit area, a mean transit time of 4 sec, a relative dispersion of 0.5, and a skewness of 0.9. $^{w}PS_{\text{cap}}$ and $^{w}PS_{\text{pc}}$ were set to 100 ml min^{-1} g^{-1}. $^{w}D_{\text{pc}}$ was set to 10^{-4} cm^{2} sec^{-1}.

Such agreement shows that the model provides correct mass balance and is a prerequisite for estimating extraction and oxygen metabolic rate from tracer kinetic data.

Zero-Order and First-Order Consumption

Shown in Fig. 4 are the nontracer oxygen concentration profiles in the RBCs and parenchymal cells with linear and zero-order consumption. With the same average oxygen consumption at 5 μmol min^{-1} g^{-1}, the axial concentration profiles were very different. With linear consumption, more oxygen is metabolized at the upstream than at the downstream end; consequently, the intracellular concentration profile is flatter than that with zero-order consumption. However, tracer kinetics showed almost no difference in the residue and outflow dilution curves (not illustrated), because they do not provide any information about where along the capillary length the oxygen was consumed. Our conclusion is that if one is interested in evaluating oxygen consumption only from tracer transients, either zero-order or first-order consumption will give the same result.

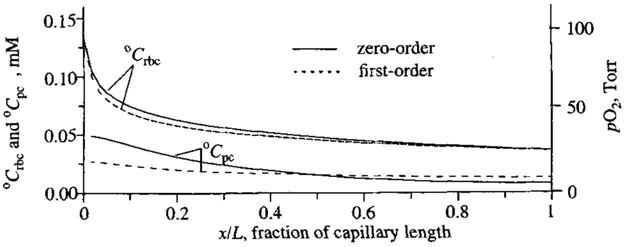

FIGURE 4. Differences in steady-state solutions when assuming zero- and first-order oxygen consumption. For linear consumption, G_{pc} = 300 ml min^{-1} g^{-1} and the average $\mathrm{MR}_{\mathrm{O}_2}$ = 5 μmol min^{-1} g^{-1}, which was the same as using zero-order consumption. Plotted were axial concentration profiles of nontracer oxygen in the RBCs (two upper curves) and parenchymal cells (two lower curves) representing the vascular and intracellular oxygen levels.

Effect of Blood Flow, Hematocrit, and Arterial $p\mathrm{O}_2$

Oxygen delivery to the exchange region is determined by three factors: capillary blood flow, hematocrit, and arterial $p\mathrm{O}_2$. These three factors affect also the axial distribution of nontracer oxygen. If one of the factors decreases while oxygen consumption remains constant, anoxia can occur. A "lethal corner" does not normally occur in the presence of axial dispersion and diffusion. Figure 5 shows the axial concentration profiles of unbound oxygen in the RBCs and parenchymal cells at different capillary blood flows. At a blood flow of 0.5 ml min^{-1} g^{-1} and with the chosen parameters, oxygen delivery by flow to the tissue was inadequate to maintain a viable $p\mathrm{O}_2$ level downstream, even though the capillary wall ($^{o}PS_{\text{cap}}$ = 200 ml min^{-1} g^{-1}) was no hindrance to oxygen delivery. As a result, the intracellular oxygen concentration fell to 0 at

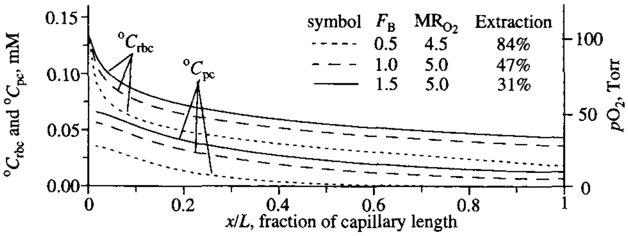

FIGURE 5. Effect of increasing the blood flow on the axial profiles of pO_2 of nontracer oxygen when consumption was uniformly constant at 5 μmol min^{-1} g^{-1}. F_B in ml min^{-1} g^{-1} was set at 0.5 (solid lines), 1.0 (long dashed lines), and 1.5 (short dashed lines). At F_B = 0.5 ml min^{-1} g^{-1}, there is "lethal corner" with pO_2 = 0 in the myocytes.

the last four-tenths of the capillary length, and the average MR_{O_2} was 4.5 μmol min^{-1} g^{-1}, which was less than the demand of 5 μmol min^{-1} g^{-1}. Note that in the flow-limited case when PS_{cap} is set infinitely large, anoxia occurs only when flow, or hematocrit, or arterial pO_2 drops to below 20% of the normal values. For tracer kinetics, as capillary blood flow (Fig. 6) or hematocrit (not illustrated) or arterial pO_2 (Fig. 7) was reduced, the retention of tracer was prolonged (there is a higher tail in the residue function), and the fraction of tracer oxygen in the outflow was reduced (there is a lower peak and higher tail in the outflow).

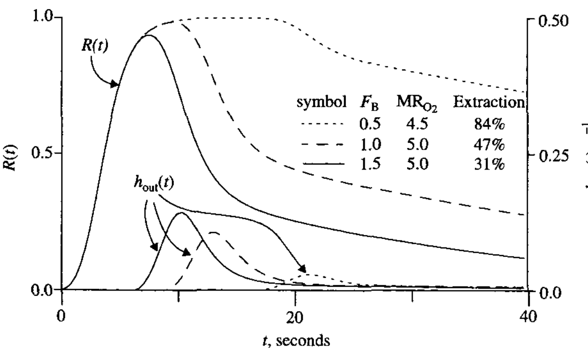

FIGURE 6. Effect of increasing blood flow on residual tracer, $R(t)$, is to shorten the retention of the tracer. The washout is earlier, and tails of the residue curves are lower at higher flows. Earlier and higher peaks in the outflow indicated less extraction and shorter mean capillary transit times.

Effect of Velocity Ratio of RBCs to Plasma

Because most oxygen is carried in the form of oxyhemoglobin in the RBCs, the mean capillary transit time is determined mainly by the RBC velocity. The higher the velocity ratio, the earlier the peak of transmitted, nonextracted oxygen appeared in the outflow. However, in the range of 1 to 2 for v_{rbc}/v_p, the effect was modest.

Effect of Intracellular Binding of Myoglobin to Oxygen

The residue and outflow dilution curves at different levels of myoglobin concentrations are shown in Fig. 8.

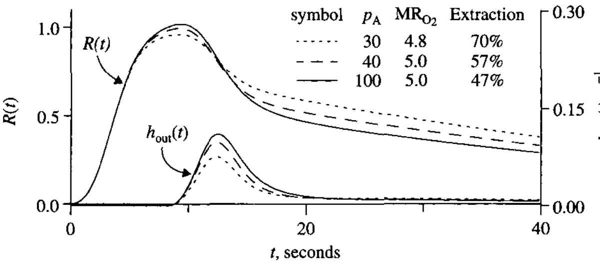

FIGURE 7. Effect of increasing the arterial pO_2 on residue and outflow curves. At the lowest arterial pO_2 of 30 torr, the average MR_{O_2} was 4.8 μmol min^{-1} g^{-1} that was less than the demand of 5 μmol min^{-1} g^{-1}. With higher inflow arterial pO_2 of 40 and 100 torr, the residue curves showed faster washout and lower tails, whereas outflow curves showed higher peaks and lower tails, indicating less fractional extraction of oxygen. However, the differences between these two were moderate, because the arterial blood was 75% and 100% saturated.

The myoglobin-oxygen binding had a buffer effect on the tracer kinetics. Myoglobin delayed the appearance of tracer in the outflow and prolonged retention. Note that zero-order consumption for this test was set at 2 μmol min^{-1} g^{-1} instead of 5 μmol min^{-1} g^{-1} order to emphasize the effect, because at a high oxygen consumption level, $°C_{pc}$ is low, below the myoglobin $p50$ and the volume of distribution, $°V''_{pc}$, approaches its maximum, Eq. 16. In this model, myoglobin concentration levels have no effect on the nontracer oxygen profiles because oxymyoglobin is in constant equilibrium with the free oxygen in parenchymal cells.

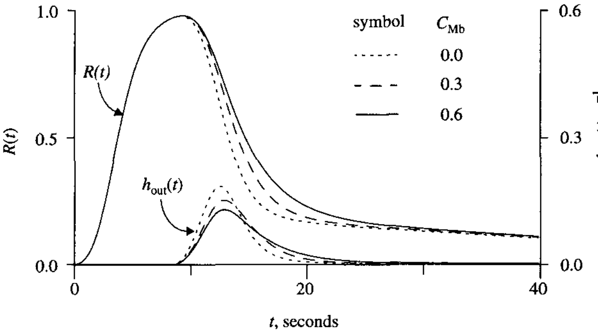

FIGURE 8. Effect of myoglobin binding on tracer residues. Myoglobin serves as a buffer in parenchymal cells. As myoglobin concentration is increased from 0 to 0.6 mM, the retention of the tracer was prolonged as indicated by the shallower downslope in residue and lower and wider peaks in outflow. Consumption is 2 μmol min^{-1} g^{-1}.

Effect of Axial Diffusion

The effect of molecular diffusion is minimal at $°D_p = 2.18 \times 10^{-5}$ cm^2 sec^{-1} (21), $°D_{rbc} = 0.95 \times 10^{-5}$ cm^2 sec^{-1} (15,42), and $°D_{pc} = 1.16 \times 10^{-5}$ cm^2 sec^{-1} (17,29). If the axial diffusion terms represent all dispersional processes, greater values than those for molecular terms must be used, even as high as 10^{-3} cm^2 sec^{-1} with

L = 0.1 cm. Figure 9 shows that high $^{o}D_{pc}$ reduced the intracellular gradient, whereas the vascular gradient was changed modestly. Note that the model is like a compartmental model when large values of D's are used. For example, when D_{pc} is large, the parenchymal cell behaves like a stirred tank.

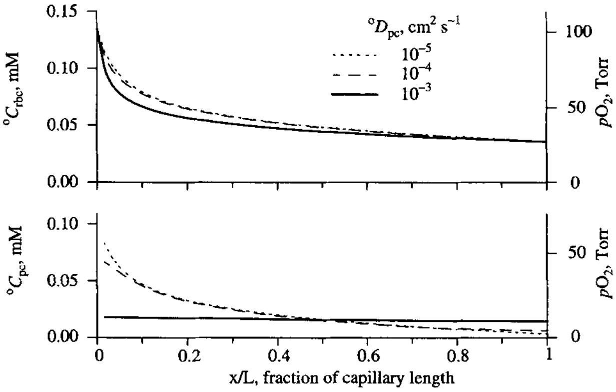

FIGURE 9. Effect of axial diffusion in parenchymal cells on the steady-state solution. A large $^{o}D_{pc}$ value produced a uniform concentration profile along the length of the parenchymal cells, whereas the axial profile in the RBCs was still steep.

Water and Oxygen Mean Transit Times

Calculated mean transit times for water and oxygen through the blood–tissue exchange unit are shown in Table 2. The effect of increasing consumption is to reduce oxygen transit time. For water produced by oxygen metabolism, the transit time to the exit is less than for water entering via the inflow, even if there is no barrier limitation. Moreover, as oxygen consumption increases, the ^{15}O-water produced from ^{15}O-oxygen reaches the outflow later. This is a consequence of the spatial distribution of sites of conversion from ^{15}O-oxygen to ^{15}O-water; at high consumption rates, more of the conversion occurs toward the upstream end of the capillary-tissue unit.

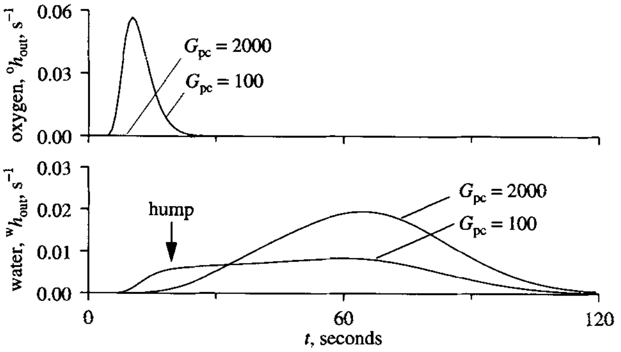

FIGURE 10. A "first-in-last-out" phenomenon for tracer water after a pulse injection of tracer oxygen. When the consumption rate is extremely high (nearly 100% extraction of oxygen, no oxygen outflow), G_{pc} = 2,000 ml min^{-1} g^{-1} and MR_{O_2} = 6.3 μmol min^{-1} g^{-1}; the transformation of oxygen to water occurs mainly at the upstream end of the capillary, thus resulting in a long mean transit time of 64 sec for water. When the consumption rate is in the normal range, G_{pc} = 100 ml min^{-1} g^{-1} and MR_{O_2} = 3.5 μmol min^{-1} g^{-1}; part of the water is generated at the downstream end of the capillary-tissue unit, and diffuses and flows out to the venous effluent more quickly, giving rise to the hump in the water curve that is only slightly delayed, compared with the oxygen outflow curve (top). The mean transit time was 54 sec. Parameters used for this simulation are F_B = 0.75 ml min^{-1} g^{-1}, Hct = 0.4; all D's are 0; $^{o}PS_{cap}$ = 1,000, $^{o}PS_{pc}$ = 1,000, $^{w}PS_{cap}$ = $^{w}PS_{pc}$ = 100 ml min^{-1} g^{-1}.

In Fig. 10, model outflow dilution curves are shown for pulse injections of ^{15}O-oxygen at the capillary entrance at low and high rates of consumption. At low MR_{O_2} the outflow $h(t)$ for water has an early hump and a late peak; the hump is due to the rapid emergence of ^{15}O-water formed at the downstream end of the capillary, and the later peak is due to the ^{15}O-water formed earlier but at points higher upstream. This is a case of "last formed, first out." At high MR_{O_2}, most of the ^{15}O-oxygen is consumed upstream and must therefore traverse the whole of the water space of the tissue, a case of "first formed, last out." These events occur because of the great difference in oxygen and water transit times.

Computational Efficiency

Solution times for a 10-segment and a 30-segment model on a SUN Sparc5 were 2.3 and 10.8 sec without axial dispersion, and 2.5 and 14.5 sec with axial dispersion. The number of function evaluations required to fit ^{15}O-oxygen PET time-activity curves of 300 sec duration using SIMPLEX are typically 100 to 150, thus requiring about 20 to 30 min for an optimization run for each region of interest (ROI) when initial estimates are poor.

RESULTS OF EXPERIMENTAL DATA ANALYSIS

The experimental curves were obtained from PET data of a beating heart of an open chest dog that was anesthetized and ventilated. Blood was sampled from the aorta and coronary sinus for measurement of the steady-state transmyocardial oxygen extraction.

Myocardial Blood Flow Measurement

To measure the blood flow, 15 mCi in ~3 ml ^{15}O-water was injected into the superior vena cava. PET (GE Advance System) was used to detect the activities in the dog heart. The images were obtained every 4 sec for the first and second minutes, every 10 sec for the third minute, and every 20 sec for the fourth and fifth minutes. The input and residue functions were obtained by placing the ROIs in the left ventricular cavity and myocardium. The myocardial blood flow was estimated using the water part of the dual model. Partial volume effects and spillover of signal from cavity to myocardium were accounted for as a part of the modeling analysis (12).

TABLE 2. Mean transit time for oxygen and water.

p_A (torr)	Oxygen Consumption	Other Conditions	$^{w}\bar{t}_{ct}$[a] (sec)	$^{o}\bar{t}_{ct}$[b] (sec)	Oxygen Extraction (%)
100	0	High *PS*'s, zero *D*'s	—	5.45	0
26	0	High *PS*'s, zero *D*'s	—	6.44	0
100	3 μmol min^{-1} g^{-1}	High *PS*'s, zero *D*'s	35.36	4.62	28
26	3 μmol min^{-1} g^{-1}	High *PS*'s, zero *D*'s	36.27	4.43	56
100	3 μmol min^{-1} g^{-1}	High *PS*'s, $^{w}D_{pc} = 0.001$ cm/sec^2	61.58	4.62	28
26	3 μmol min^{-1} g^{-1}	High *PS*'s, $^{w}D_{pc} = 0.001$ cm/sec^2	61.38	4.43	56
100	3 μmol min^{-1} g^{-1}	$^{w}PS_{pc} = 2$ ml min^{-1} g^{-1}, zero *D*'s	67.81	4.62	28
26	3 μmol min^{-1} g^{-1}	$^{w}PS_{pc} = 2$ ml min^{-1} g^{-1}, zero *D*'s	68.63	4.43	56

[a] $^{w}\bar{t}_{cap} = 4.35$ sec; $^{w}\bar{t}_{ct} = 59.45$ sec, *if water is carried in from the arterial inflow.*
[b] $^{o}\bar{t}_{cap} = 3.37$ sec with or without consumption.

Myocardial Oxygen Consumption

About 80 mCi of ^{15}O-oxygen was introduced via ventilation within three breaths. The images were obtained every 2 sec for the first minute, then every 4 sec for the second minute, then every 10 sec for the third minute, and then every 20 sec for the fourth and fifth minutes. The time-activity curves were obtained from the same ROIs used for the ^{15}O-water. We fitted the myocardial PET signal to the model-generated residue function plus the PET signal from the left ventricular cavity (input function) scaled by the spillover ratio. Because the objective was to estimate the oxygen consumption, we reduced the degrees of freedom in the modeling by optimizing on as few parameters as possible. The *PS*'s can be combined because they are in series and have reciprocal relations. Therefore, in fitting the model to the experimental data, we optimized on only four parameters: $^{o}PS_{cap}$, G_{pc} assuming first-order consumption, $^{w}PS_{pc}$, and the spillover ratio (in the same style as for the estimation of flow). Other *PS* values were set to high values so that the solutions are insensitive to them.

An Example of MR_{O_2} Estimation on the Whole Left Ventricle

Analysis of PET ROI time-activity curves for ^{15}O-water during control state gave an estimated left ventricular flow of 1.1 ml min^{-1} g^{-1}. From ^{15}O-oxygen curves, the estimated MR_{O_2} for the left ventricle was 3.2 μmol min^{-1} g^{-1}. The directly measured global oxygen consumption of the whole heart by the Fick method was 2.9 μmol min^{-1} g^{-1}. Fig. 11 shows that the model curve fitted well to the PET signal with a coefficient of variation of 8.3%. The calculated venous pO_2 was 32 torr, compared with the observed 35 torr; the average extraction was 34%.

DISCUSSION

Generality of the Model

The model is general and is a good vehicle for gaining insights into oxygen transport in microcirculation. Many model parameters are adjustable, to set up different physiological and pathological conditions. For example, one can look at the oxygen distribution in tissues in normoxia, hypoxic hypoxia (low arterial pO_2), and anemic hypoxia (low hematocrit). Furthermore, the model partially, if not completely, answered the questions raised by our previous linear model concerning nonlinearity of hemoglobin and myoglobin binding to oxygen and different velocities of RBCs and plasma (see *Results of Computer Simulation*). The possible effects of even spatial distributions of mitochondria and red cell spacing on oxygen exchange (20,27,28) are not addressed in the current model. These, however, both result in diminished oxygen transport, compared with the current model and can therefore be roughly approximated by reductions in *PS*'s.

Computational Speed

The motivation to develop this nonlinear model was to model the kinetics of ^{15}O-oxygen in PET studies for esti-

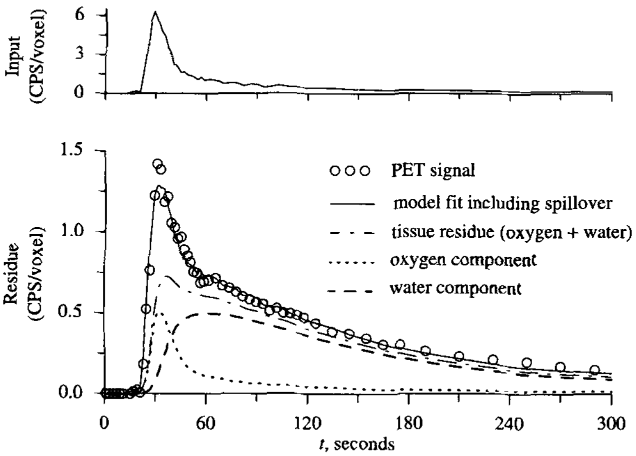

FIGURE 11. Analysis of PET ^{15}O-oxygen residue curves from an open-chest dog study during the control state. Model parameters in ml min^{-1} g^{-1}: $^{o}PS_{cap} = 362$ $G_{pc} = 74$ and $^{w}PS_{pc} = 0.96$. Left ventricular cavity to myocardial spillover ratio = 12%.

mating oxygen consumption regionally. To achieve the computational efficiency that is critical to the analysis of experimental data, different algorithms for nontracer and tracer-labeled oxygen were implemented to solve the speed problem caused by the nonlinear features of the model, primarily the binding of oxygen to hemoglobin and myoglobin. For tracer transients, the binding processes are taken into account by using the virtual volumes of distribution that are dependent on the nontracer concentrations. Once the steady-state solution is obtained, the virtual volumes can be calculated and remain constant throughout the tracer transient. This is similar to our previous linear model (19) from the point of view of modeling tracer kinetics. However, there are two *major* improvements: (i) the nontracer oxygen levels in different regions are calculated based on the given arterial pO_2 and model parameters, not approximated as in the linear model; and (ii) the axial gradients of nontracer oxygen concentration are used to calculate the local virtual volumes along the capillary length, whereas the linear model uses average oxygen levels and virtual volumes. In summary, the present model maintains fast computation and yet is more accurate in the sense that both nontracer and tracer oxygen transport and metabolism are determined by the same set of model parameters.

The solution times for the linear analysis of the transients increase as the square of the number of axial segments chosen; thus, it is useful to reduce the number of segments to the minimum acceptable for accuracy. Likewise, because the calculations for axial dispersion are separated from those for radial exchanges, one can gain a 26% reduction in solution time for $N_{seg} = 30$ by setting the D's to 0, bypassing the computation. Because data are best fitted by including high D's to account for extravascular dispersion due to the anatomical arrangements of microvascular units, setting them to 0 requires a compromise to obtain correct shapes for the curves. This can be accomplished by using unrealistically low values for the *PS*'s, which must be regarded as shaping factors for the purpose of data fitting and do not represent true values for barrier *PS*'s. We emphasize that this has nothing to do with linear *versus* nonlinear modeling, but rather is an issue in the modeling of data on indicators that are flow-limited, or nearly so, in their blood–tissue exchange (5,6,11) and contrasts with earlier, low estimates of the PS's (43).

Fitting the Model to the Experimental Residue Curve

In PET studies, only the tracer residue function can be obtained from the PET scan data. Our objective is to estimate oxygen consumption by fitting the model to the residue function. Neither the identifiability nor the physiological accuracy of individual model parameters, such as the *PS*'s, are of primary concern because obtaining a correct estimate of MR_{O_2} is the primary goal. To gain speed and to illustrate the principle, the D's were set to 0 and the PS's used (at unrealistically low values) as shaping factors to fit the curves. To assess the error of the MR_{O_2} estimate, we generated pseudodata with and without noise added, then fit the model to these artificial pseudodata curves, which have exactly known parameters. In generating the pseudodata, zero-order consumption was used and MR_{O_2} was set at 5 μmol min^{-1} g^{-1}. $^{o}PS_{cap}$ and $^{w}PS_{pc}$ were set at 200 and 1 ml min^{-1} g^{-1}. A random number generator was used to produce uniformly distributed noise with a 0 mean and a standard deviation of 20% of the value at each time point. The noise was then added proportionally to the clean data to generate 30 noisy curves.

The model was fitted to both clean and noisy "pseudodata" (as defined in Table 3) with three parameters: $^{o}PS_{cap}$, $^{w}PS_{pc}$, and the consumption term (V_{max} for Michaelis-Menten kinetics or G_{pc} for linear consumption). Initial values were randomly selected, and 30 cases were tested for four different settings (*i.e.*, clean or noisy data using Michaelis-Menten kinetics or linear consumption). Table 3 shows the means and standard deviations of estimated model parameters, MR_{O_2} and the coefficient of variation of the model fit. The model solutions fit the clean data nearly perfectly, whereas a coefficient of variation of 22% ± 1.9% for the noisy data was in accord with the 20% noise added. All four settings gave excellent estimates of MR_{O_2} ranging from 4.95 to 5.09 μmol min^{-1} g^{-1}. The *SD*'s of parameters for the noisy data were three times those for the clean pseudodata.

The striking fact is that even with 20% proportional noise, the *SD* of MR_{O_2} was only ~5% of the mean. Having

TABLE 3. Stability of estimating oxygen consumption from "pseudodata" tissue residue curves (*n* = 30 trials).

Data Type[a]	MR_{O_2}	CV[b] (%)	$^{o}PS_{cap}$	$^{w}PS_{pc}$	V_{max}	G_{pc}
Clean	5.03 ± 0.08	0.3 ± 0.4	193 ± 15	1.1 ± 0.2	5.07 ± 0.20	
Clean	4.95 ± 0.08	0.4 ± 0.4	200 ± 13	1.2 ± 0.3		297 ± 45
Noisy	5.09 ± 0.27	22.0 ± 1.9	245 ± 121	1.9 ± 1.4	5.42 ± 0.74	
Noisy	4.97 ± 0.21	22.0 ± 1.9	251 ± 113	1.7 ± 1.2		314 ± 125

[a] Clean = model solution with no added noise; for definitions of other terms, see Table 1. Noisy = model solution + 20% proportional random noise added.
[b] CV = coefficient of variation.

an estimation method with little sensitivity to noise is important in PET or nuclear magnetic resonance studies where noise is unavoidable. Because noise increases with reduction in the size of the ROIs (voxel sizes), such insensitivity is critical to obtaining information with high spatial resolution. Another observation was that either Michaelis-Menten kinetics or first-order consumption could be used to estimate MR_{O_2} with no significant difference.

The identifiability of individual model parameters is, however, problematic when noise is involved. From Table 3, the *PS*'s, V_{max}, and G_{pc} estimated from the noisy data had biased means and large *SD*'s even though MR_{O_2} was estimated with adequate accuracy. For Michaelis-Menten kinetics, the mean of V_{max} was 5.42 μmol min^{-1} g^{-1}, which was larger than the mean estimated MR_{O_2} of 5.09 μmol min^{-1} g^{-1}, indicating that the intracellular oxygen concentration was less than saturation in downstream locations. Observations of residue functions can probably not be used to distinguish linear from nonlinear processes in tracer experiments done during conditions in steady-state for nontracer solutes.

With respect to the conductance parameters, the sensitivity functions of $^{o}PS_{cap}$ and G_{pc} on the residue curve are very similar with linear consumption (Fig. 12). Thus, $^{o}PS_{cap}$ and G_{pc} may not be separable in curve fitting, and various combinations of $^{o}PS_{cap}$ and G_{pc} give similar model fits. The inverse of the sum of $1/^{o}PS_{cap}$ and $1/G_{pc}$ was relatively constant for all 30 cases (118.63 ± 3.22 ml min^{-1} g^{-1}), indicating the linear processes of transmembrane transport and consumption are in series. This observation serves to emphasize the point that these conductances, the *PS*'s and the G_{pc}, serve as shaping factors and that the MR_{O_2} estimation is not very dependent on their relative values, but rather depends on the transformation of ^{15}O-oxygen to ^{15}O-water (*i.e.*, material balance between the oxygen with its short transit time and water with its long transit time). For this particular case, the mean transit time for ^{15}O-oxygen is 4.3 sec, whereas that for ^{15}O-water is 77 sec. In summary, with a single residue curve, the MR_{O_2} estimate can be obtained with satisfactory accuracy, but the individual parameters for permeation and reaction for oxygen are not clearly distinguishable. This requires both residue and outflow detection (19).

Grieb *et al.* (23) initiated a modeling analysis of outflow dilution curves for ^{18}O-oxygen in their study of the exchange of oxygen between blood and brain tissue. Although they said that their modeling analysis was incomplete, they pointed out that the transit times for the nonextracted oxygen were dependent on the consumption rate, as we have shown. Furthermore, they ascertained that the blood-brain barrier was so permeable to oxygen, because of its high lipid solubility (50), that it could not be recognized as a resistance to oxygen transport, and declined to give any estimate of the barrier PS product. Their careful analyses thus led them, even without having accomplished the full modeling, to the same conclusions that we have reached here. We can therefore regard our work as affirming their conclusions. It is true that our studies are on the heart, not the brain, which makes the situation even more interesting because it has long been recognized that the blood-brain barrier has a much lower permeability to hydrophilic solutes than the cardiac capillary. This all makes good sense, because not only is oxygen much more lipid-soluble than water, but also even water is flow-limited in its transport through the heart (5).

CONCLUSIONS

This model describes physiologically realistic features of oxygen transport and metabolism in the microcirculation. It is rather general and is widely applicable to measuring oxygen consumption in other organs. The model parameters can be varied to simulate different physiological states. Tracer transients can be computed efficiently, and the model is useful for routine data analysis. Preliminary results show that it is a promising model for estimating oxygen consumption from myocardial residue curves obtained by PET.

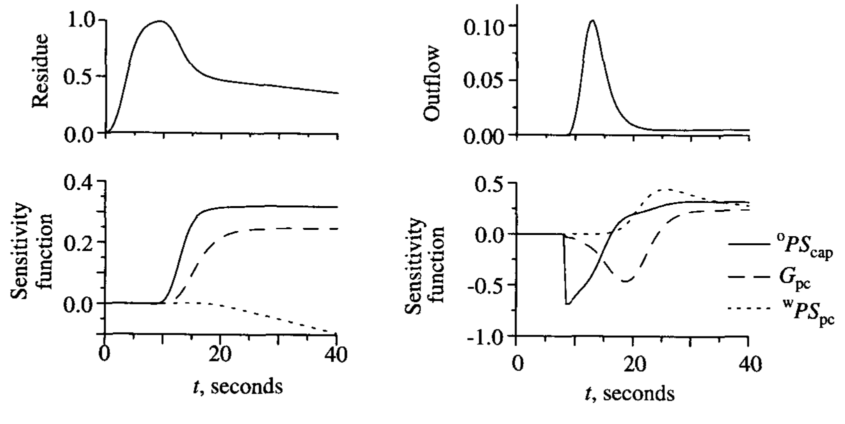

FIGURE 12. Sensitivity functions of G_{pc} (first order), $^{o}PS_{cap}$, and $^{w}PS_{pc}$ on the residue (left) and outflow (right) curves. MR_{O_2} = 5 μmol min^{-1} g^{-1}, G_{pc} = 270, $^{o}PS_{cap}$ = 190 ml min^{-1} g^{-1}, and $^{w}PS_{pc}$ = 1 ml min^{-1} g^{-1}. The sensitivity functions are defined as $[\delta f(t)]/f(t)/[\delta p_i/p_i]$, where $f(t)$ is the model function $R(t)$ or h(t), and p_i is the *i*th parameter.

REFERENCES

1. Bassingthwaighte, J. B., F. H. Ackerman, and E. H. Wood. Applications of the lagged normal density curve as a model for arterial dilution curves. *Circ. Res.* 18:398–415, 1966.
2. Bassingthwaighte, J. B. Plasma indicator dispersion in arteries of the human leg. *Cir. Res.* 19:332–346, 1966.
3. Bassingthwaighte, J. B., T. J. Knopp, and J. B. Hazelrig. A concurrent flow model for capillary-tissue exchange. In: Capillary permeability (Alfred Benzon Symp. II), edited by C. Crone and N. A. Lassen. Copenhagen: Munksgaard, 1970, pp. 60–80.
4. Bassingthwaighte, J. B., T. Yipintsoi, and R. B. Harvey. Microvasculature of the dog left ventricular myocardium. *Microvasc. Res.* 7:229–249, 1974.
5. Bassingthwaighte, J. B. Physiology and theory of tracer washout techniques for the estimation of myocardial blood flow: flow estimation from tracer washout. *Progr. Cardiovasc. Dis.* 20:165–189, 1977.
6. Bassingthwaighte, J. B., and C. A. Goresky. Modeling in the analysis of solute and water exchange in the microvasculature. In: Handbook of physiology, sect. 2. The cardiovascular system, vol. IV. The microcirculation, edited by E. M. Renkin and C. C. Michel. Bethesda, MD: American Physiological Society, 1984, pp. 549–626.
7. Bassingthwaighte, J. B., R. B. King, and S. A. Roger. Fractal nature of regional myocardial blood flow heterogeneity. *Circ. Res.* 65:578–590, 1989.
8. Bassingthwaighte, J. B., C. Y. Wang, and I. S. Chan. Blood-tissue exchange via transport and transformation by endothelial cells. *Circ. Res.* 65:997–1020, 1989.
9. Bassingthwaighte, J. B., M. A. Malone, T. C. Moffett, R. B. King, I. S. Chan, J. M. Link, and K. A. Krohn. Molecular and particulate depositions for regional myocardial flows in sheep. *Circ. Res.* 66:1328–1344, 1990.
10. Bassingthwaighte, J. B., I. S. Chan, and C. Y. Wang. Computationally efficient algorithms for capillary convection-permeation-diffusion models for blood-tissue exchange. *Ann. Biomed. Eng.* 20:687–725, 1992.
11. Bassingthwaighte, J. B., and D. A. Beard. Fractal ^{15}O-water washout from the heart. *Circ. Res.* 77:1212–1221, 1995.
12. Bergmann, S. R., P. Herrero, J. Markham, C. J. Weinheimer, and M. N. Walsh. Noninvasive quantitation of myocardial blood flow in human subjects with oxygen-15–labeled water and positron emission tomography. *J. Am. Coll. Cardiol.* 14:639–652, 1989.
13. Bohr, C. Uber die spezifische tatigkeit der lungen bei der respiratori schen gasaufnahme und ihr verhalten zu der durch die alveolarwand stafffindenden gasdiffusion. *Skand. Arch. Physiol.* 22:221–280, 1909.
14. Buerk, D. G., and Bridges, E. W. A simplified algorithm for computing the variation in oxyhemoglobin saturation with pH, pCO_2, T, and DPG. *Chem. Eng. Commun.* 47:113, 1986.
15. Clark, A., Jr., W. J. Federspiel, P. A. A. Clark, and G. R. Cokelet. Oxygen delivery from red cells. *Biophys. J.* 47: 171–181, 1985.
16. Clough, A. V., A. Al-Tinawi, J. H. Linehan, and C. A. Dawson. Regional transit time estimation from image residue curves. *Ann. Biomed. Eng.* 22:128–143, 1994.
17. de Koning, L., J. C. Hoofd, and F. Kreuzer. Oxygen transport and the function of myoglobin. Theoretical model and experiments in chicken gizzard smooth muscle. *Pflügers Arch.* 389:211–217, 1981.
18. Desjardins, C., and B. R. Duling. Microvessel hematocrit: measurement and implications for capillary oxygen transport. *Am. J. Physiol.* 252:H494–H503, 1987.
19. Deussen, A., and J. B. Bassingthwaighte. Modeling ^{15}O-oxygen tracer data for estimating oxygen consumption. *Am. J. Physiol.* 270(*Heart Circ. Physiol.* 39):H1115–H1130, 1996.
20. Federspiel, W. J., and I. H. Sarelius. An examination of the contribution of red cell spacing to the uniformity of oxygen flux at the capillary wall. *Microvasc. Res.* 27:273–285, 1984.
21. Goldstick, T. K., V. T. Ciuryla, and L. Zuckerman. Diffusion of oxygen in plasma and blood. *Adv. Exp. Med. Biol.* 75:183–190, 1976.
22. Gonzalez, F., and J. B. Bassingthwaighte. Heterogeneities in regional volumes of distribution and flows in the rabbit heart. *Am. J. Physiol.* 258(*Heart Circ. Physiol.* 27):H1012–H1024, 1990.
23. Grieb, P., R. E. Forster D, Strome, C. W. Goodwin, and P. C. Pape. O_2 exchange between blood and brain tissues studied with $^{18}O_2$ indicator-dilution technique. *J. Appl. Physiol.* 58:1929–1941, 1985.
24. Groebe, K., and G. Thews. Theoretical analysis of oxygen supply to contracted skeletal muscle. *Adv. Exp. Med. Biol.* 200:495–514, 1986.
25. Groebe, K., and G. Thews. Effects of red cell spacing and red cell movement upon oxygen release under conditions of maximally working skeletal muscle. In: Oxygen transport to tissue XI, edited by K. Rakusan, G. P. Biro, T. K. Goldstick, and Z. Turek. New York: Plenum Press, 1989, pp. 175–185.
26. Grunewald, W. A., and W. Sowa. Capillary structures and O_2 supply to tissue. An analysis with a digital diffusion model as applied to the skeletal muscle. *Rev. Physiol. Biochem. Pharmacol.* 77:149–209, 1977.
27. Hellums, J. D. The resistance to oxygen transport in the capillaries relative to that in the surrounding tissue. *Microvasc. Res.* 13:131–136, 1977.
28. Hellums, J. D., P. K. Nair, N. S. Huang, and N. Ohshima. Simulation of intraluminal gas transport processes in the microcirculation. *Ann. Biomed. Eng.* 24:1–24, 1996.
29. Homer, L. D., J. B. Shelton, C. H. Dorsey, and T. J. Williams. Anisotropic diffusion of oxygen in slices of rat muscle. *Am. J. Physiol.* 246(*Reg. Int. Comp. Physiol.* 15):R107–R113, 1984.
30. Huang, S. C., D. G. Feng, and M. E. Phelps. Model dependency and estimation reliability in measurement of cerebral oxygen utilization rate with oxygen-15 and dynamic positron emission tomography. *J. Cereb. Blood Flow Metab.* 6:105–119, 1986.
31. Hudson, J. A., and D. B. Cater. An analysis of factors affecting tissue oxygen tension. *Proc. R. Soc. Lond.* B161:247, 1964.
32. King, R. B., J. B. Bassingthwaighte, J. R. S. Hales, and L. B. Rowell. Stability of heterogeneity of myocardial blood flow in normal awake baboons. *Circ. Res.* 57:285–295, 1985.
33. King, R. B., G. M. Raymond, and J. B. Bassingthwaighte. Modeling blood flow heterogeneity. *Ann. Biomed. Eng.* 24: 352–372, 1996.
34. Krogh, A. The number and distribution of capillaries in muscles with calculations of the oxygen pressure head necessary for supplying the tissue. *J. Physiol.* 52:409–415, 1919.
35. Napper, S. A., and R. W. Schubert. Mathematical evidence for flow-induced changes in myocardial oxygen consumption. *Ann. Biomed. Eng.* 16:349–365, 1988.
36. Page, E., L. P. McCallister, and B. Power. Stereological measurements of cardiac ultrastructures implicated in exci-

tation-contraction coupling. *Proc. Natl. Acad. Sci. U.S.A.* 68:1465–1466, 1971.

37. Page, E., and L. P. McCallister. Quantitative electron microscopic description of heart muscle cells. *Am. J. Cardiol.* 31:172–181, 1973.
38. Popel, A. S. Analysis of capillary-tissue diffusion in multicapillary systems. *Math. Biosci.* 39:187–211, 1978.
39. Popel, A. S. Theory of oxygen transport to tissue. *Crit. Rev. Biomed. Eng.* 17:257–321, 1989.
40. Raichle, M. E., R. L. Grubb, Jr., J. O. Eichling, and M. M. Ter-Pogossian. Measurement of brain oxygen utilization with radioactive oxygen-15: experimental verification. *J. Appl. Physiol.* 40:638–640, 1976.
41. Reneau, D. D., D. F. Bruley, and M. H. Knisely. A mathematical simulation of oxygen release, diffusion, and consumption in the capillaries and tissue of the human brain. In: Chemical engineering in medicine and biology. New York: Plenum Press, 1967, pp. 135–241.
42. Riveros-Moreno, V., and J. B. Wittenberg. The self-diffusion coefficients of myoglobin and hemoglobin in concentrated solutions. *J. Biol. Chem.* 247:895–901, 1972.
43. Rose, C. P., C. A. Goresky, and G. G. Bach. The capillary and sarcolemmal barriers in the heart: an exploration of labeled water permeability. *Circ. Res.* 41:515–533, 1977.
44. Rose, C. P., and C. A. Goresky. Limitations of tracer oxygen uptake in the canine coronary circulation. *Circ. Res.* 56:57–71, 1985.
45. Singh, M. P., M. Sharan, and A. Aminataei. Development of mathematical formulae for O_2 and CO_2 dissociation curves in the blood. *IMA J. Math. Appl. Med. Biol.* 6:25–46, 1989.
46. Taegtmeyer, H. Carbohydrate interconversions and energy production. *Circulation* 72(Suppl. IV):1–8, 1985.
47. Tangelder, G. J., D. W. Slaaf, A. M. M. Muijtjens, T. Arts, M. G. A. oude Egbrink, and R. S. Reneman. Velocity profiles of blood platelets and red blood cells flowing in arterioles of the rabbit mesentery. *Circ. Res.* 59:505–514, 1986.
48. Ter-Pogossian, M. M., J. O. Eichling, D. O. Davis, and M. J. Welch. The measure *in vivo* of regional oxygen utilization by means of oxyhemoglobin labeled with radioactive oxygen-15. *J. Clin. Invest.* 49:381–391, 1970.
49. Ter-Pogossian, M. M., and P. Herscovith. Radioactive oxygen-15 in the study of cerebral blood flow, blood volume, and oxygen metabolism. *Semin. Nucl. Med.* 15:377–394, 1985.
50. Thews, G. Die Sauerstoffdiffusion im Gehirn. Ein Betrag lur Frage der Sauerstroffversorgung der Organe. *Pflügers Arch.* 271:197, 1960.
51. Wittenberg, B. A., and J. B. Wittenberg. Transport of oxygen in muscle. *Ann. Rev. Physiol.* 51:857–878, 1989.
52. Zierler, K. L. A critique of compartmental analysis. *Ann. Rev. Biophys. Bioeng.* 10:531–562, 1981.
53. Adair, G. S., The hemoglobin system. VI The oxygen dissociation curve of hemoglobin. *J. Biol. Chem.* 63:529, 1925.
54. Yipintsoi, T., P. D. Scanlon, and J. B. Bassingthwaighte. Density and water content of dog ventricular myocardium. *Proc. Soc. Exp. Biol. Med.* 141:1032–1035, 1972.
55. Safford, R. E., E. A. Bassingthwaighte, and J. B. Bassingthwaighte. Diffusion of water in cat ventricular myocardium. *J. Gen. Physiol.* 72:513–538, 1978.

NOMENCLATURE

See Table 1 for terminology and abbreviations.